ACS APPLIED MATERIALS & INTERFACES

Research Article

www.acsami.org

Novel Zirconium Nitride and Hydroxyapatite Nanocomposite Coating: Detailed Analysis and Functional Properties

A. Joseph Nathanael,[†,‡] R. Yuvakkumar,[‡] Sun Ig Hong,[*,‡] and Tae Hwan Oh[*,†]

[†]Department of Nano, Medical and Polymer Materials, Yeungnam University, Gyeongsan 712-749, S. Korea

[‡]Department of Nanomaterials Engineering, Chungnam National University, Daejeon 305-764, S. Korea

ABSTRACT: A new type of high-quality zirconium nitride (ZrN) and hydroxyapatite (HA) bionanocomposite was prepared by radio-frequency (RF) magnetron sputtering for biomedical applications. Detailed analysis of this composite coating revealed that a higher substrate temperature (ST) (>300 °C) increased its crystallinity, uniformity, and functional properties. This nanocomposite showed some encouraging functional properties. Mechanical analyses of the nanocomposite showed improved hardness, modulus, and wear resistance, which were found to be due to the increasing volume fraction of ZrN at higher ST. Biomineralization and in vitro cell analysis revealed increased weight gain and enhanced cell activity with increased substrate temperature. Overall, the results of the present study indicate that this nanocomposite coating could become a promising alternative for biomedical applications.

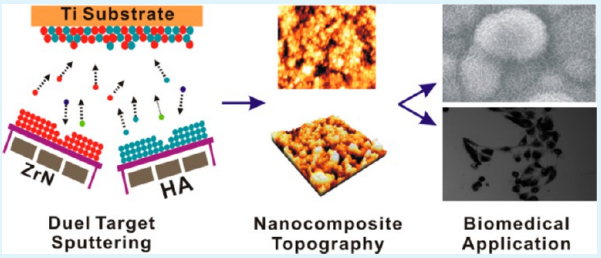

KEYWORDS: *hydroxyapatite, nanocomposite, biomaterial, friction coefficient, biomineralization, bioactivity*

1. INTRODUCTION

A wide variety of biomaterials are currently used in various diagnostic and therapeutic devices in a range of fields including orthopedics, dentistry, and ophthalmology. Accordingly, a great number of attempts have been made to increase the lifetimes of implants and improve their performance, many of which have focused on protective coatings. The surface characteristics of protective coatings have been enhanced or modified by expanded structures and compositions, enabling their use in various applications. Composite materials have recently attracted a great deal of attention because of their diversified properties. Normally, protective coatings used as biomedical implant materials have specific characteristics such as low modulus of elasticity, high chemical stability and wear resistance, low friction coefficient, good adhesion to the substrate, and good biocompatibility.[1−3]

Transition-metal nitride films such as TiN, CrN, and ZrN exhibit an unusual combination of physical and chemical properties, which has led to their extensive use in many industrial applications for corrosion resistance, decorative coatings, cutting tools, and diffusion barriers in microelectronics. Their attractive physical properties include golden color, high hardness, good thermal stability, and low electrical resistivity.[4] In recent years, ZrN coatings have been extensively applied in industry owing to their excellent mechanical properties,[5,6] golden color,[7] and good corrosion resistance[8] relative to conventional TiN coatings.[9] However, few studies have been carried out to investigate the biomedical applications of ZrN coatings.[10] Nevertheless, their use on medical implant materials has been drawing attention owing to their biocompatibility, excellent corrosion resistance, good lubricity, high hardness, and ductility.[11,12]

Hydroxyapatite [HA, $Ca_{10}(PO_4)_6(OH)_2$] is a well-known biomaterial comprising major inorganic components of teeth and bone. HA is mainly used for bone tissue regeneration because of its excellent biocompatible nature,[13] as well as reinforcing fillers for biocomposites.[14] Despite its encouraging biological properties, the poor mechanical properties of HA have hindered its clinical applications. Formations of composites with other materials increase the strength of HA,[15−17] and some hybrids or composite coatings and nanostructured coatings on metals have further improved its usefulness for specific applications.[16−18] Many structural analyses of ZrN and HA coatings are available; however, no such studies of ZrN/HA composite coatings or potential biomedical applications have been conducted to date.

In this study, we prepared novel ZrN/HA nanocomposite coatings using the radio-frequency (RF) magnetron sputtering method by changing the substrate temperatures while maintaining other parameters at constant values to expand our previous study[19] in which various deposition times (60 and 120 min) and substrate temperatures (200 and 400 °C) were investigated. We found that the optimum power and working pressure for the production of ZrN/HA nanocomposite films were 200 W and 1.86 Pa, respectively. At lower powers, the deposition rate was very low, and at different working pressures, the sputtering was not efficient. Therefore, we fixed these

Received: April 18, 2014
Accepted: June 4, 2014
Published: June 4, 2014

   dx.doi.org/10.1021/am5023557 | ACS Appl. Mater. Interfaces 2014, 6, 9850−9857

conditions along with the deposition time (120 min) and changed the ST to identify the optimum ST for producing ZrN/HA thin films for biomedical applications. Finally, we analyzed the developed nanocomposite coatings using various methods.

2. MATERIALS AND METHODS

2.1. Preparation of ZrN/HA Nanocomposite Coatings. ZrN/HA nanocomposite samples were deposited on commercially pure (cp) titanium substrates that had been prepared and cleaned as described elsewhere.[19] An RF magnetron cosputtering system (SNTEK, RSP-5003 series) was used to prepare the ZrN/HA nanocomposite coatings using 3-in.-diameter HA and ZrN targets. During deposition, a constant working pressure of 1.86 Pa was maintained in the sample chamber under an argon atmosphere. The base pressure in the deposition chamber was about 8×10^{-6} Pa, and the RF power applied to the targets was 200 W. In this study, we varied the ST [room temperature (RT) and 100, 200, 300, and 400 °C] while maintaining a constant coating time of 120 min. The targets were presputtered for 10 min by applying an RF power of 100 W under an Ar atmosphere before sample preparation. A schematic diagram of the sputtering mechanism is shown in Figure 1. In

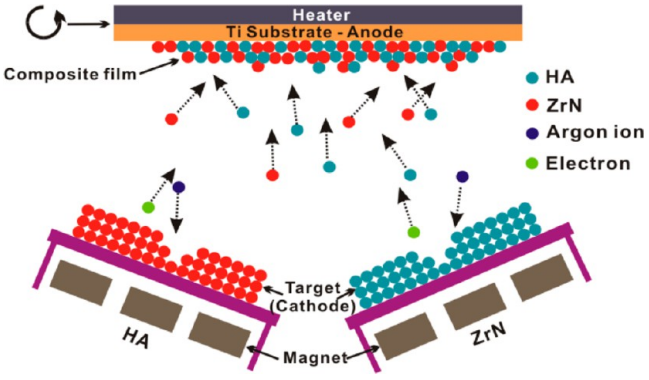

Figure 1. Schematic diagram of the dual-target sputtering mechanism.

sputtering, target surfaces are bombarded by high-energy gaseous ions under high-voltage acceleration, which leads to the ejection of atoms from the target surface (sputtering) that are propelled toward the substrate. This would then form a thin film on the substrate.[20] For sputtering, the kinetic energy of the energetic particles should much higher than conventional thermal energies.

2.2. Characterization. ZrN/HA nanocomposite coatings were analyzed by X-ray diffraction (XRD; Rigaku, D/MAX 2500H) to identify their structures. Additionally, morphological variations in the deposition were analyzed by field-emission scanning electron microscopy (FESEM; Helios 600). Finally, transmission electron microscopy (TEM, Tecnai F30 S-Twin) was conducted for further in-depth analysis of the nanocomposite coating. TEM samples were prepared by the focused ion beam (FIB) technique, and cross-sectional TEM images were obtained.

Atomic force microscopy (AFM; psia XE-100) was used to evaluate the topography and roughness of the coating. The hardness and modulus of the nanocomposite coating were examined by nano-indentation (Nanoindenter XP). A wear test was carried out using a wear test analyzer (Tribometer). For this analysis, SS balls, 3 mm in diameter were slid against the film at a normal load of 2 N and a sliding speed of 50 mm/s. The biomineralization ability of the nanocomposite-coated surface was examined by immersing the substrate in simulated body fluid (SBF) for different time periods. The cell viability of different ZrN/HAp composite coatings was evaluated using human osteosarcoma cell line MG-63. A detailed description of the experimental methods and conditions is provided in our previous report.[13] Five samples were tested for each culture period to improve the data statistics.

3. RESULTS AND DISCUSSION

3.1. X-ray Diffraction (XRD) Analysis. Phase analysis of the ZrN/HA nanocomposite coating was carried out by XRD.

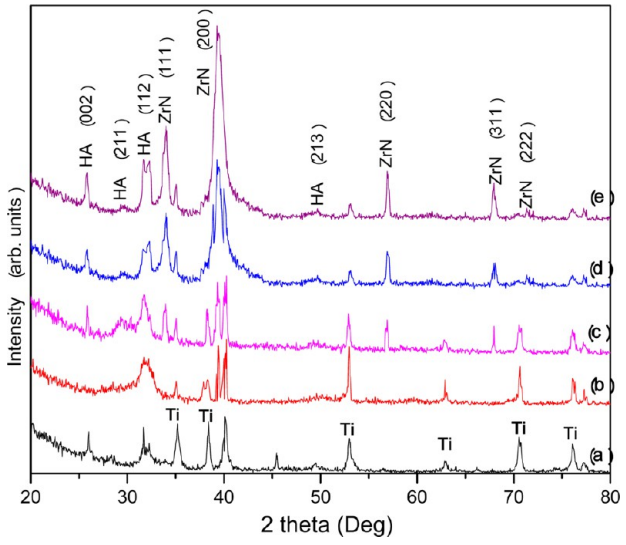

Figure 2. XRD patterns of HA/ZrN nanocomposite coatings prepared at different substrate temperatures: (a) RT and (b) 100, (c) 200, (d) 300, and (e) 400 °C.

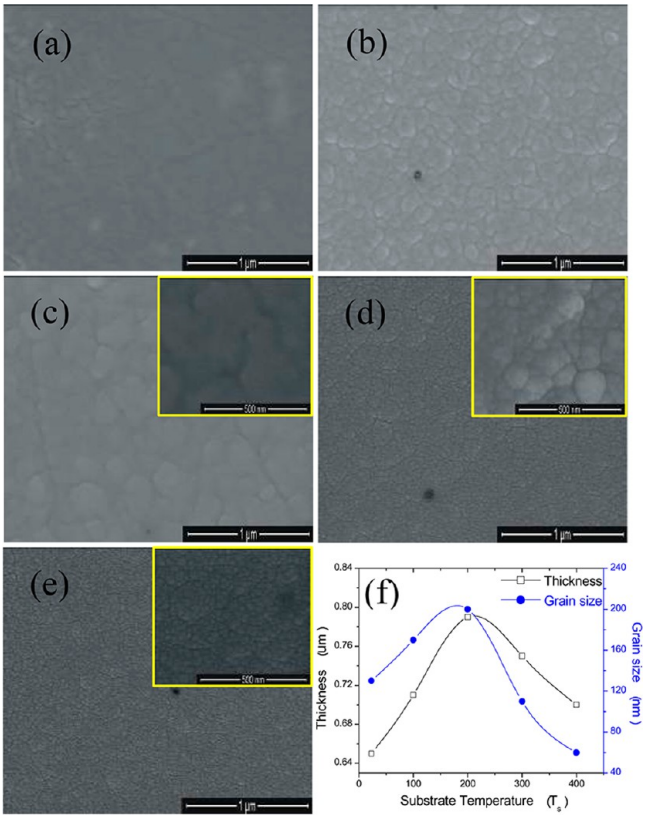

Figure 3. SEM images of HA/ZrN nanocomposite coatings prepared at different substrate temperatures: (a) RT and (b) 100, (c) 200, (d) 300, and (e) 400 °C. (f) Thickness and grain size variations as functions of substrate temperature based on FESEM analysis.

Figure 2 shows the XRD patterns of the nanocomposite coatings deposited on the Ti substrate by the cosputtering

dx.doi.org/10.1021/am5023557 | ACS Appl. Mater. Interfaces 2014, 6, 9850−9857

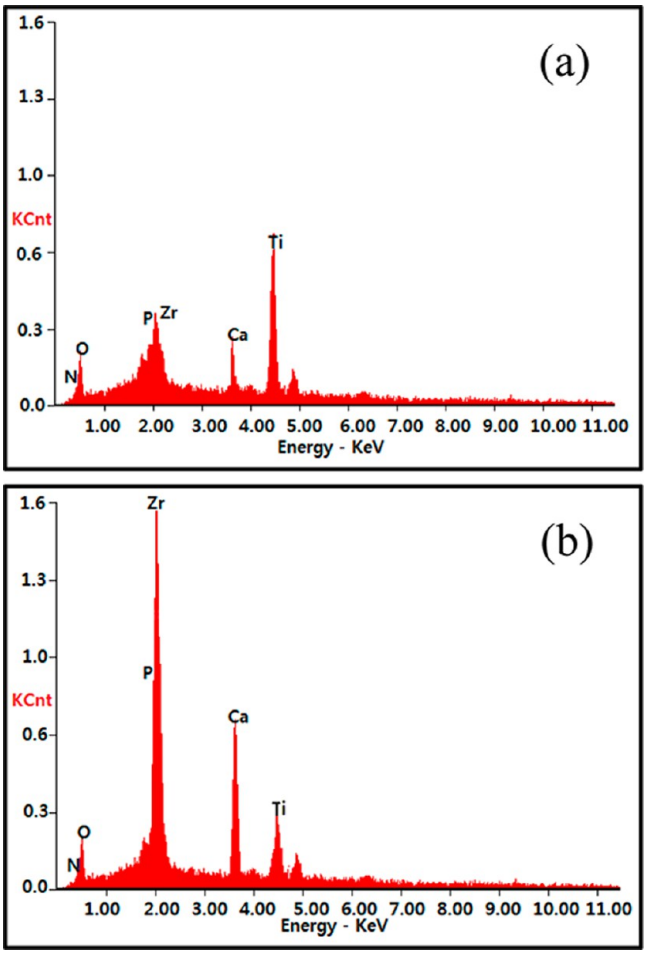

Figure 4. EDX analysis of HA/ZrN nanocomposite coatings prepared at (a) 100 and (b) 400 °C.

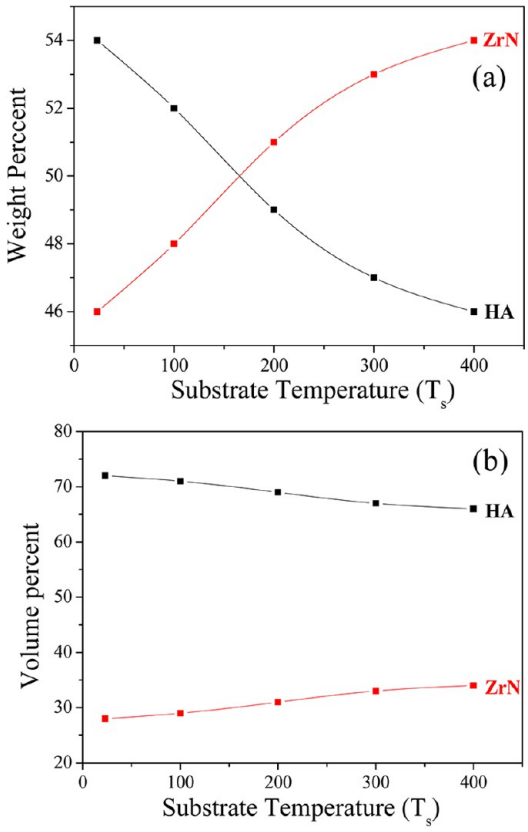

Figure 5. (a) Weight and (b) volume percentages of HA/ZrN nanocomposite coatings prepared at different substrate temperatures.

method at different STs. The diffraction peaks are attributed to the HAp and ZrN phases. Some Ti peaks were also observed by XRD. The intensities of the ZrN and HA peaks obviously increased with increasing ST. According to our observations, substrate temperature primarily influences the characteristics of the coating. At less than 100 °C, the peaks of the HA and ZrN phases were very weak, possibly because the very thin coating layer resulted in mainly the substrate peaks being observed (Figure 2a). When the substrate temperature was increased to 200−300 °C, the XRD peak intensity increased, suggesting that the crystallinity changed with the ST (Figure 2b,c). At 400 °C, well-pronounced peaks of apatite and ZrN were observed. As shown in Figure 2d, the substrate Ti peak was weak under these coating conditions, suggesting the successful formation of a ZrN and HA composite coating layer.

Cubic-phase ZrN reflections corresponding to the (111), (200), (220), (311), and (222) planes and hexagonal apatite reflections corresponding to the (002), (211), (300), and (202) planes were prominent, but other minor apatite peaks were barely visible for higher STs. As the ST increased above 200 °C, fairly sharp and strong performance for the ZrN (200) plane was detected in all XRD patterns (Figure 2d), indicating that ZrN prepared at this temperature had the preferred orientation. In Figure 2, strong peaks mainly from cubic ZrN and hexagonal apatite were observed, and no other major peaks were visible, indicating the formation of mainly HA/ZrN composite coating. It has been reported that,[21] for pure ZrN coatings, lower STs result in high contamination with unreacted zirconium impurities. In the present study, we used a pure ZrN target instead of a Zr target in nitrogen atmosphere, so the elemental Zr level was negligible, if there was any, in the composite coatings even at lower STs. The ZrN(200) and ZrN(111) peaks were prominent compared to other peaks, and the intensity of the ZrN peaks increased more significantly with increasing ST, suggesting an increasing volume fraction of ZrN. The changes in the HA(002) and HA(211) peaks with ST were not as pronounced as those in the ZrN peaks.

3.2. Electron Microscopy Analysis. The FESEM images shown in Figure 3 provide clear insight into the morphology of the ZrN/HA nanocomposite coatings. Variations in morphology were observed with changes in ST. Specifically, the coatings produced at RT and the lower STs were very thin, whereas the thickness increased with increasing ST. The coating produced at RT showed a snowy appearance and some large grains; however, the grain size decreased considerably as the ST increased. Indeed, at an ST of 100 °C, the average grain size was 120 ± 12 nm, whereas at 400 °C, it was 85 ± 15 nm. The change in grain size with respect to ST is shown in Figure 3f.

Panels a and b of Figure 4 display the EDS spectra from the HA/ZrN nanocomposite coatings deposited at substrate temperatures of 100 and 400 °C, respectively. With increasing substrate temperature, the Zr and Ca peaks increased significantly, reflecting the increased thickness of the HA/ZrN nanocomposite coating at 400 °C. The Ti peak was from Ti substrate, and it decreased with increasing HA/ZrN nanocomposite coating thickness at 400 °C. Because no major XRD peaks other than those for ZrN and HA were observed from the composite coating in Figure 2, the Zr and Ca

dx.doi.org/10.1021/am5023557 | ACS Appl. Mater. Interfaces 2014, 6, 9850−9857

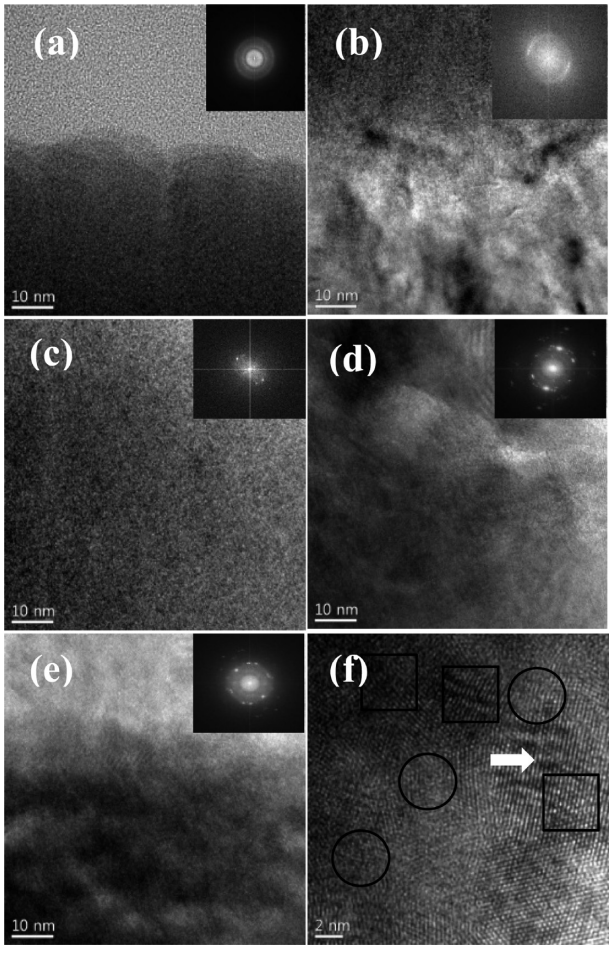

Figure 6. TEM micrograph of HA/ZrN nanocomposites coatings prepared at different substrate temperatures: (a) RT and (b) 100, (c) 200, (d) 300, and (e) 400 °C. (f) HRTEM image of the sample shown in panel e.

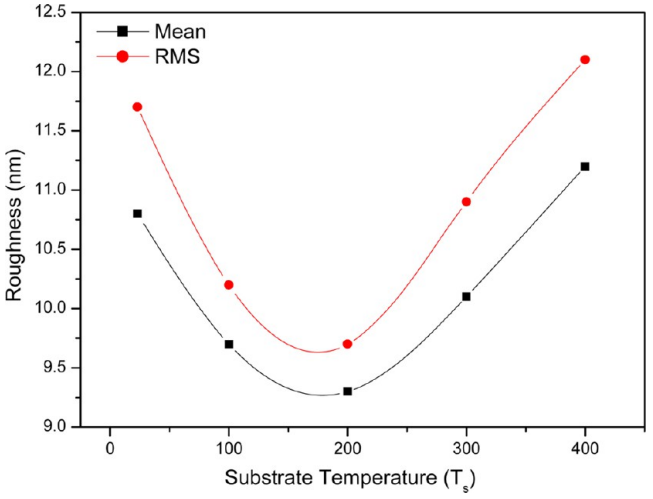

Figure 8. Mean and rms roughness values of ZrN/HA nanocomposite coatings prepared at different substrate temperatures.

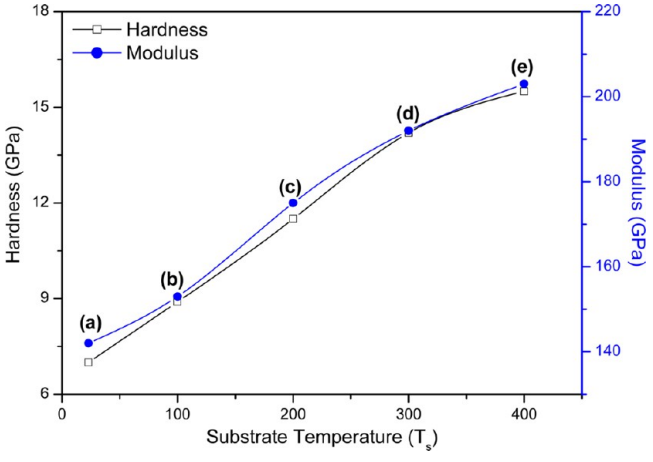

Figure 9. Hardness and modulus values of HA/ZrN composite coatings prepared at different substrate temperatures: (a) RT and (b) 100, (c) 200, (d) 300, and (e) 400 °C.

EDS peaks are most likely from ZrN and HA, respectively. Based on the XRD analysis confirming the presence of ZrN and

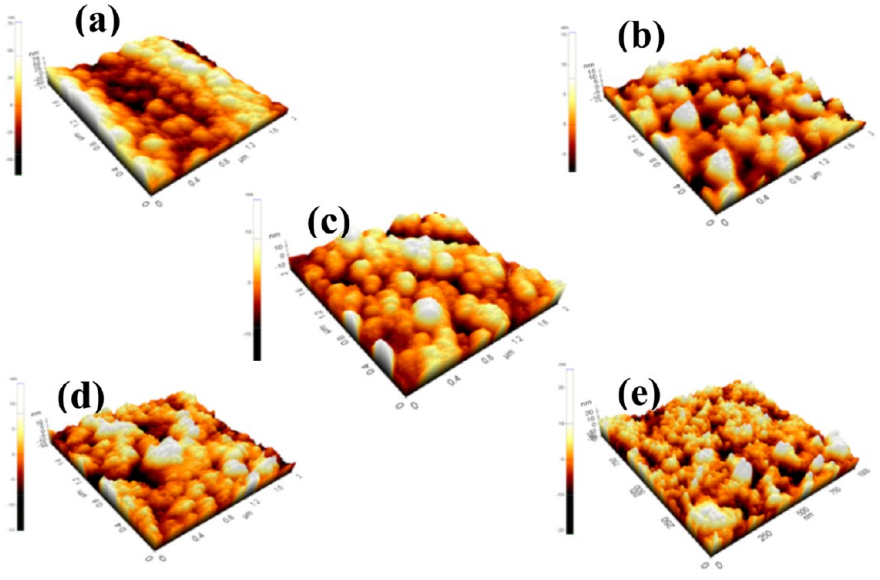

Figure 7. Three-dimensional AFM images of HA/ZrN nanocomposites coating prepared at different substrate temperatures: (a) RT and (b) 100, (c) 200, (d) 300, and (e) 400 °C.

dx.doi.org/10.1021/am5023557 | ACS Appl. Mater. Interfaces 2014, 6, 9850−9857

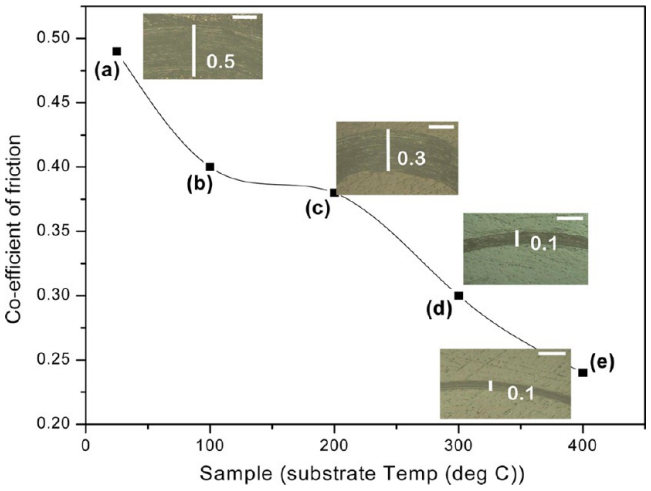

Figure 10. Variation in friction coefficient with number of laps on ZrN/HA composite coatings for samples prepared at different substrate temperatures: (a) pure Ti and (b) 100, (c) 200, (d) 300, and (e) 400 °C. The insets show the corresponding OM images of the wear tracks (values in millimeters, 200×, scale bar = 0.22 mm).

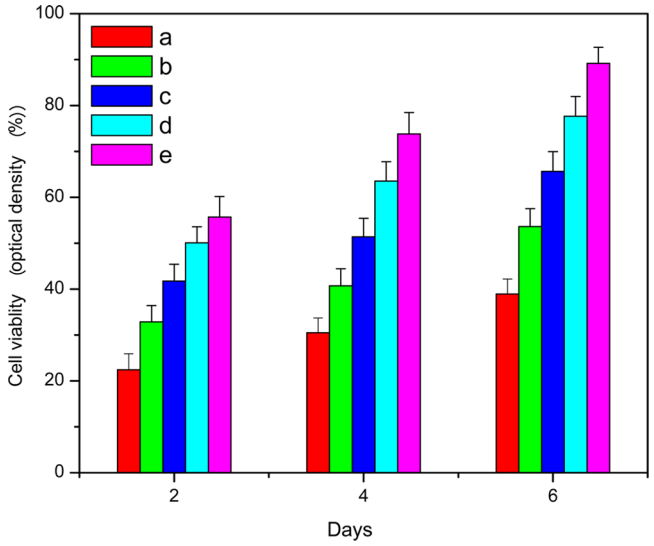

Figure 12. MG-63 cell viability on different samples after different incubation periods: (a) RT and (b) 100, (c) 200, (d) 300, and (e) 400 °C.

HA, the weight and volume fractions of ZrN and HA were determined from the composition data obtained by EDS analysis.

Panels a and b of Figure 5 display the changes in the weight and volume fractions, respectively, of ZrN and HA. As shown in Figure 5a, the weight fraction of HA was slightly greater than that of ZrN at low substrate temperatures and became lower above an ST of 200 °C. Because the sputtering yield is dependent on the mass of atoms, the difference in weight fractions between ZrN and HA is not significant. In Figure 5b, the volume fraction of HA was observed to be far greater than that of ZrN because of its lower density. Nevertheless, the volume fraction of ZrN increased from 0.28 to 0.33 as the ST increased from room temperature to 400 °C. The increasing volume fraction of ZrN with increasing ST in Figure 5 is consistent with the increasing ZrN XRD peaks observed in Figure 2. The reason for the increasing volume fraction of ZrN with increasing substrate temperature is not clear, although higher temperature might enhance the formation and stability of ZrN.[21] Larijani et al.[21] suggested that the nucleation and growth of ZrN increased with increasing temperature up to 500 °C in sputtered ZrN coating. Liao et al.[22] reported that hydroxyapatite lost adsorbed and lattice water in its structure as the temperature was increased from 25 to 400 °C, resulting in weight loss. The decrease in the HA weight and volume fractions can be attributed to the loss of structural water in HA.[22] Caution should be exercised in analyzing the exact volume fraction using EDS data because EDS is considered to be insufficiently accurate to calculate the exact compositions of compounds. Because the change of ZrN volume fraction with ST in Figure 5b is significant, the volume fraction data in Figure 5b are thought to give some meaningful insight into the effect of substrate temperature on the ZrN volume fraction.

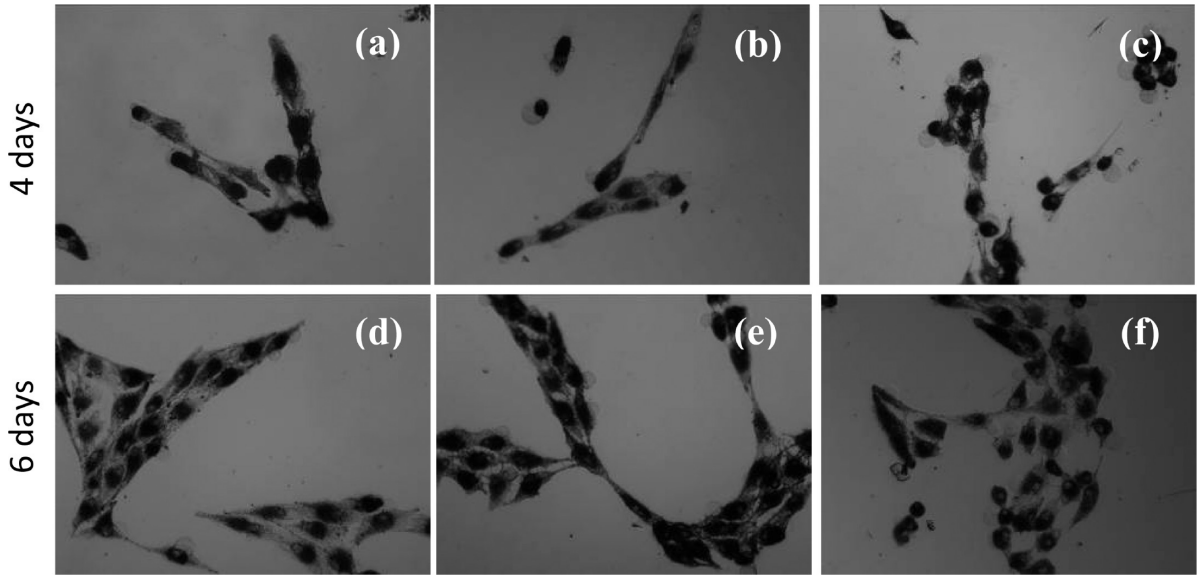

Figure 11. Optical images of the MG-63 cells grown at substrate temperatures of (a,d) 200, (b,e) 300, and (c,f) 400 °C for different time periods.

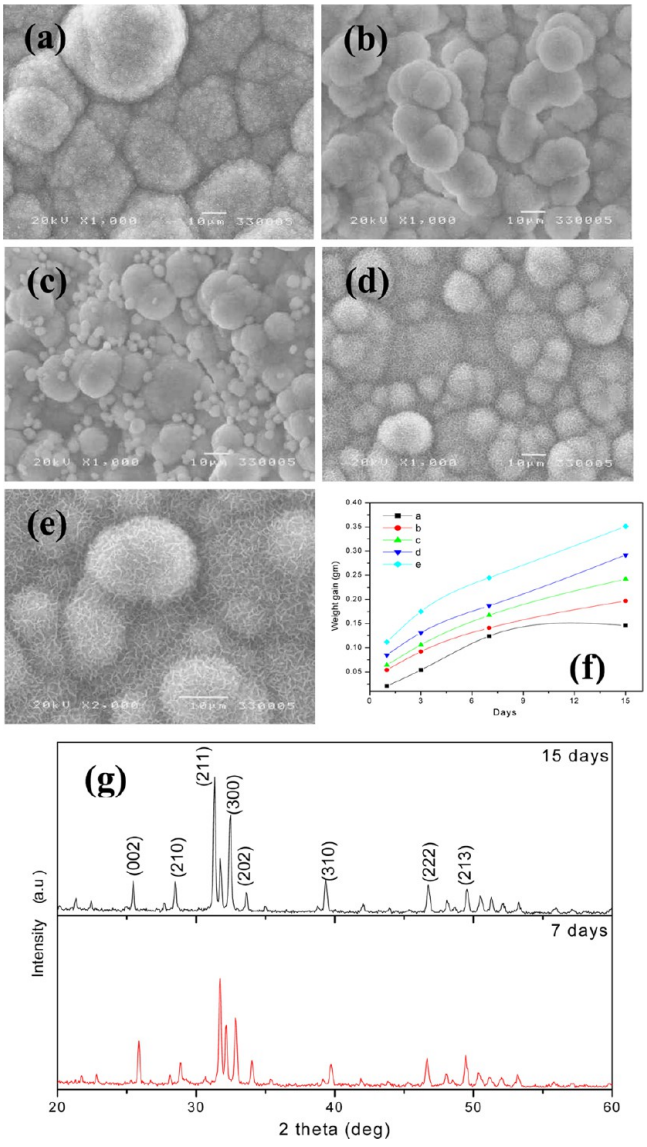

Figure 13. SEM analysis of the biomineralization ability of the coating: (a) RT and (b) 100, (c) 200, (d) 300, and (e) 400 °C after 15 days of immersion in the SBF. (f) Weight gains by the samples after different time periods. (g) XRD patterns of the sample shown in panel e after 7 and 15 days of immersion in SBF.

Further insight into the ZrN/HA composite coating was obtained by high-resolution (HR) TEM analysis. As shown in Figure 3, HRTEM micrographs of the ZrN/HA composite films revealed varying nanostructural features with different STs. The nanocomposite films produced at RT and 100 °C showed an amorphous structure (Figure 6a). Additionally, the HRTEM image indicated that the ZrN and HA coatings were distributed evenly along the surfaces. Furthermore, as shown in the inset of the figure, the fast Fourier transform (FFT) pattern of the sample nanocomposite coating confirmed that the ST highly influences the crystallinity of the coating. Specifically, as the ST increased, the crystallinity of the coating also increased considerably, with the sample generated at 400 °C showing better crystallinity than the other samples. Finally, the ZrN particles were found to have better crystallinity than the HA particles.

As shown in Figure 6b, deposition at STs of RT and 100 °C led to planar structures, without any well-defined microstructure. This micrograph, along with the X-ray results shown in Figure 2, indicates that the film consisted of ZrN and HA. The crystalline phase with clear lattice fringes in Figure 6d appears to be the ZrN phase. The X-ray diffraction pattern shows the formation of nanocomposites in this film. This appears to be supported by the FFT pattern, which can be indexed by both the HA (less crystalline) and ZrN (highly crystalline) lattices. The micrograph also reveals a homogeneous microstructure of nearly equiaxial grains. The average grain size in the film was 22 nm, so the microstructure of the composite coating was nanocrystalline. Such an observation further supports the results of X-ray diffraction.

Figure 6e shows a TEM micrograph of the film deposited at 400 °C. Preparation at this ST resulted in a finer microstructure relative to that of the sample prepared at lower ST. Additionally, the grain sizes were more homogeneously distributed and smaller than 10 nm. The TEM results for this film are consistent with the results of XRD analysis, in terms of phase formation and grain size.

During thin film deposition, grain growth normally occurs at higher ST due to enhanced adatom mobility. However, the opposite trend was observed in the present study. This might have been due to desorption of adatoms at higher STs because the adsorption energy was greater than the surface energy at higher temperatures.[23,24] Heavy agglomeration was not found in the FESEM images of the samples generated at higher temperatures, supporting the tendency toward desorption of adatoms at higher STs. Agglomeration of crystallites at higher temperatures is mainly due to the increasing mobility of adatoms.[23,24] Deposition at a higher ST also induces desorption and the elimination of pores and voids, leading to decreased coating thickness.[23,24]

Lattice fringes are clearly visible in the HRTEM image of the sample generated at 400 °C (Figure 6f) (indicated by the arrow). The sputtered film with the crystalline nature is ZrN, whereas the less crystalline film is HA, supporting the results of the XRD analysis. TEM analysis of the sample formed at 400 °C further confirmed these findings. It clearly showed the polycrystalline nature of the film. Small grains of about 5−10 nm in size with clear lattice fringes were randomly oriented in a less crystalline matrix (see Figure 6f, circles). Further analysis of the HRTEM images confirmed that there was a dislocation between the ZrN and HA phases (Figure 6f, squares).

3.3. Atomic Force Microscopy (AFM) Analysis. Surface topographies obtained by AFM for the nanocomposite coatings are illustrated in Figure 7. The surfaces of samples formed using lower substrate temperatures appear smooth and dense and feature domed columnar grains. For the RT film, an rms roughness value of 11.7 was measured. Granular structures were seen on the surfaces of samples formed at lower STs. As the ST increased, the roughness initially decreased and then increased, reaching 12.1 nm at 400 °C. The composite film exhibited a distinctively different surface structure for different STs. Specifically, films formed at lower temperatures (RT and 100 °C) had an overall granular morphology and the presence of uneven valleys and hills. However, increasing the substrate temperature led to a dramatic decrease in grain size. This was manifested by the RT film, which exhibited a distinct surface topography from a composite film. At 300 °C, the cubic ZrN phase emerged, resulting in the film displaying a cauliflowerlike surface due to the increasing density of domes (Figure 7d). At this ST, the subdomes in each cauliflower became finer than

those in the lower-ST films, and the roughness started increasing.

With further increases in ST (400 °C), coarsening and roughening of the film surfaces was observed (Figure 7e). The surfaces of these films were formed by elongated domes, and the diameters of the domes decreased with increasing ST, causing the domelike elongated grains to appear sharper. Even though no agglomeration was observed, the surface showed some uneven valleys and hills. The domelike hills contains elongated grains, which completely alters the topography and may ultimately increase the surface roughness of the film. Additionally, the volume fraction of ZrN increased with increasing temperature, which might also influence the change in roughness with increasing temperature. The mean and rms roughness values of the different samples are given in Figure 8.

3.4. Mechanical Properties of the Nanocomposite Coating. The hardness, elastic modulus, and friction coefficient values of the composite coatings were determined by nanoindentation and wear testing. The results clearly demonstrated that the mechanical properties were dependent on the ST. As shown in Figure 9, the hardness and elastic modulus of the composite coating increased significantly with increasing ST. The hardness was only around 7 GPa when the ST was RT and reached a maximum value of 15.5 GPa at an ST of 400 °C. When the ST was increased, the modulus value also increased from 138 to 200 GPa.

It should be noted that the hardness and elastic modulus of the composite coating were higher than those of the pristine HA thin film because of the hardness contribution of ZrN. The greater hardness of composite coatings with higher elastic modulus can be attributed to the thicker dense layer of the composite coating and the increasing fraction of ZrN at higher temperature. XRD analyses (Figure 2) revealed that the intensity of the ZrN peaks increased more with temperature than that of the HA peaks, which did not change much with temperature above 200 °C, suggesting that the volume fraction of ZrN increased with temperature.[25] The volume fraction analyses based on the EDS data also suggested an increase in ZrN volume fraction with increasing ST. The increasing volume fraction of ZrN and the stabilized dense ZrN/HA nanostructure can enhance the hardness and modulus with increasing ST.

The wear rate of the coating was determined based on the friction coefficient using a wear test analyzer (Figure 10). When compared to the uncoated Ti plates, the composite-coated samples showed increased wear resistance, with samples formed at higher STs exhibiting better wear resistance than the other samples. The sample prepared at 400 °C exhibited a higher wear resistance than any other samples. The wear tracks shown in the optical micrographs (OMs) confirm the performance of the samples in the test. The wear resistance generally increased with increasing hardness.[26]

3.5. Bioactivity Analysis. The biocompatibility and bioactivity of materials used for bone tissue engineering applications have primarily been evaluated using MG-63 osteosarcoma cell lines.[27] Therefore, in this study, we cultured MG-63 cells on HA/ZrN nanocomposite samples and assessed their morphology and cell density. The cell growth morphology was analyzed by optical micrograph. Figure 11 shows the good attachment and homogeneous growth of MG-63 cells on the nanocomposite coatings. In all samples, the cells grew in a dense layer, indicating good attachment and growth of cells. Observations at higher magnification revealed that the cells expressed polygonal and slightly elongated morphologies, which is typical of MG-63 cells. The osteoblast adhesion was significantly higher for samples prepared at an ST of 400 °C than for those prepared at lower STs. Additionally, the optical density of the cell growth was analyzed by lactate dehydrogenase (LDH) assay. The cell proliferation rate showed a similar tendency for all samples tested. As shown in Figure 12, the optical density of the cells continued to increase throughout the 6-day experiment for all samples, with a 4−5-fold increase in adherent cell numbers occurring in all groups.

As explained above, increasing ST was found to change the crystallinity, surface morphology, grain size, topography, and roughness of the nanocomposite films. These surface-chemistry and grain-size changes apparently led to improved cell behavior. The grain sizes of the samples formed at STs fo 300 and 400 °C were less than 100 nm, which increased the surface areas of the coatings and, therefore, the interaction between the osteoblasts and the coating surface. The surface roughness was altered for ZrN/HA composite coatings with changing ST. The experimental mean and rms roughness values of different samples influence cell attachment and might also explain the good attachment of MG-63 cells.

3.6. Biomineralization Ability. The biomineralization ability of the ZrN/HA composite coating was determined by immersing the coated substrate in SBF solution for different lengths of time (1, 3, 7, and 15 days) and then incubating the sample, during which the solution was changed every day. Newly formed apatite was observed on the surface in the presence of SBF. SEM results after 1, 3, 7 (not shown here), and 15 days of immersion in SBF indicated HA formation on all samples (Figure 13). Moreover, HA formation increased with time, and all surfaces were completely covered after 3 days. These findings were confirmed by XRD analysis of the samples. Additionally, the spectra revealed the disappearance of Ti and ZrN phases and the appearance of almost all apatite phases with higher peak intensities.

The weight gains of the substrates due to deposition of mineralized particles from the SBF solution was used to analyze the biomineralization ability of the coating. The coatings formed using higher substrate temperatures showed greater weight gain and biomimetic appearance relative to the other coatings. It is interesting to note that the apatite deposition in SBF increased on the ZrN/HA coating formed at the highest substrate temperatures (>300 °C), despite the increasing volume fraction of ZrN, suggesting that nanostructured ZrN/HA composite induces apatite deposition significantly in SBF. As discussed in the microstructural analysis, higher-temperature substrates form fine composite grains with uniform distributions, higher crystallinity, and nanostructured grains. This can also lead to increased biomineralization ability of these specific samples.[28] The higher-ST samples clearly present the apatite morphology. Finally, based on numerous series of experiments, we are able to provide the optimum conditions for ZrN/HA nanocomposite coating as follows: deposition time, 120 min; ST, 400 °C; working pressure, 1.86 Pa; RF power, 200 W.

4. CONCLUSIONS

The effects of substrate temperature on the crystallinity, surface morphology, microstructure, topography, and roughness of a new type of ZrN/HA nanocomposite thin films were investigated. The results revealed that crystallinity increased with increasing substrate temperature, but thickness and grain size initially increased and then decreased with increasing temperature. The roughness of the coating showed the

opposite trend. Functional properties of the nanocomposite coating were determined by analyzing its mechanical and bioactive nature. The hardness and modulus increased with increasing substrate temperature, whereas the friction coefficient decreased, suggesting that the mechanical strength of the coating was better at higher substrate temperature. Similarly, the bioactivity and biomineralization ability of the nanocomposite coating was higher when higher substrate temperatures were used.

AUTHOR INFORMATION

Corresponding Authors

*E-mail: sihong@cnu.ac.kr (S.I.H.).
*E-mail: taehwanoh@ynu.ac.kr (T.H.O.).

Notes

The authors declare no competing financial interest.

ACKNOWLEDGMENTS

This research was supported by the Fundamental R&D Programs for Core Technology of Materials (2013) and by the Yeungnam University research grants in 2014.

REFERENCES

(1) Shen, Z.; Adolfsson, E.; Nygren, M.; Gao, L.; Kawaoka, H.; Niihara, K. Dense Hydroxyapatite−Zirconia Ceramic Composites with High Strength for Biological Applications. *Adv. Mater.* **2001**, *13*, 214−216.

(2) Wu, C.; Chen, Z.; Yi, D.; Chang, J.; Xiao, Y. Multidirectional Effects of Sr-, Mg-, and Si-Containing Bioceramic Coatings with High Bonding Strength on Inflammation, Osteoclastogenesis, and Osteogenesis. *ACS Appl. Mater. Interfaces* **2014**, *6*, 4264−4276.

(3) Nathanael, A. J.; Lee, J. H.; Mangalaraj, D.; Hong, S. I.; Rhee, Y. H. Multifunctional Properties of Hydroxyapatite/Titania Bio-Nano-Composites: Bioactivity and Antimicrobial Studies. *Powder Technol.* **2012**, *228*, 410−415.

(4) Park, Y. G.; Wey, M. Y.; Hong, S. I. Enhanced Wear and Fatigue Properties of Ti−6Al−4V Alloy Modified by Plasma Carburizing/CrN Coating. *J. Mater. Sci: Mater. Med.* **2007**, *18*, 925−931.

(5) Rizzo, A.; Signore, M. A.; Mirenghi, L.; Tapfer, L.; Piscopiello, E.; Salernitano, E.; Giorgi, R. Sputtering Deposition and Characterization of Zirconium Nitride and Oxynitride Films. *Thin Solid Films* **2012**, *520*, 3532−3538.

(6) Huang, J. H.; Ho, C. H.; Yu, G. P. Effect of Nitrogen Flow Rate on the Structure and Mechanical Properties of ZrN Thin Films on Si(1 0 0) and Stainless Steel Substrates. *Mater. Chem. Phys.* **2007**, *102*, 31−38.

(7) Budke, E.; Krempel-Hesse, J.; Maidhof, H. Decorative Hard Coatings with Improved Corrosion Resistance. *Surf. Coat. Technol.* **1999**, *112*, 108−113.

(8) Wiiala, U. K.; Penttinen, I. M.; Korhonen, A. S.; Aromaa, J.; Ristolainen, E. Improved Corrosion Resistance of Physical Vapour Deposition Coated TiN and ZrN. *Surf. Coat. Technol.* **1990**, *41*, 191−204.

(9) Qi, Z. B.; Zhu, F. P.; Wu, Z. T.; Liu, B.; Wang, Z. C.; Peng, D. L.; Wu, C. H. Influence of Yttrium Addition on Microstructure and Mechanical Properties of ZrN Coatings. *Surf. Coat. Technol.* **2013**, *231*, 102−106.

(10) Wang, G.; Zreiqat, H. Functional Coatings or Films for Hard-Tissue Applications. *Materials* **2010**, *3*, 3994−4050.

(11) Chou, W. J.; Yu, G. P.; Huang, J. H. Corrosion Resistance of ZrN Films on AISI 304 Stainless Steel Substrate. *Surf. Coat. Technol.* **2003**, *167*, 59−67.

(12) Moon, B. H.; Choe, H. C.; Brantley, W. A. Surface Characteristics of TiN/ZrN Coated Nanotubular Structure on the Ti−35Ta−*x*Hf Alloy for Bio-Implant Applications. *Appl. Surf. Sci.* **2012**, *258*, 2088−2092.

(13) Nathanael, A. J.; Hong, S. I.; Mangalaraj, D.; Ponpandian, N.; Chen, P. C. Template Free Growth of Novel Hydroxyapatite Nanorings: Formation Mechanism and Their Enhanced Functional Properties. *Cryst. Growth Des.* **2012**, *12*, 3565−3574.

(14) Nathanael, A. J.; Hong, S. I.; Mangalaraj, D.; Chen, P. C. Large Scale Synthesis of Hydroxyapatite Nanospheres by High Gravity Method. *Chem. Eng. J.* **2011**, *173*, 846−854.

(15) Nathanael, A. J.; Mangalaraj, D.; Chen, P. C.; Ponpandian, N. Mechanical and Photocatalytic Properties of Hydroxyapatite/Titania Nanocomposites Prepared by Combined High Gravity and Hydrothermal Process. *Compos. Sci. Technol.* **2010**, *70*, 419−426.

(16) Nathanael, A. J.; Mangalaraj, D.; Ponpandian, N. Controlled Growth and Investigations on the Morphology and Mechanical Properties of Hydroxyapatite/Titania Nanocomposite Thin Films. *Compos. Sci. Technol.* **2010**, *70*, 1645−1651.

(17) Nathanael, A. J.; Mangalaraj, D.; Chen, P. C.; Ponpandian, N. Nanostructured Leaf Like Hydroxyapatite/TiO_2 Composite Coatings by Simple Sol−Gel Method. *Thin Solid Films* **2010**, *518*, 7333−7338.

(18) López, E. O.; Mello, A.; Sendão, H.; Costa, L. T.; Rossi, A. L.; Ospina, R. O.; Borghi, F. F.; Silva Filho, J. G.; Ross, A. M. Growth of Crystalline Hydroxyapatite Thin Films at Room Temperature by Tuning the Energy of the RF-Magnetron Sputtering Plasma. *ACS Appl. Mater. Interfaces* **2013**, *5*, 9435−9445.

(19) Nathanael, A. J.; Lee, J. H.; Hong, S. I. Effect of Processing Parameters on the Mechanical Reliability of ZrN/Hydroxyapatite Nanocomposite Coatings. *Adv. Sci. Lett.* **2012**, *15*, 285−290.

(20) Thian, E. S.; Choong, C. Magnetron Sputtering Deposition of Chemically Modified Hydroxyapatite. In *Hydroxyapatite Coatings for Biomedical Applications*; Zhang, S., Ed.; CRC Press: Boca Raton, FL, 2013; Chapter 1, pp 6−7.

(21) Larijani, M. M.; Kiani, M.; Tanhayi, M.; Majdabadi, A. Characterization of Ion Beam Sputtered ZrN Coatings Prepared at Different Substrate Temperatures. *Cryst. Res. Technol.* **2011**, *46*, 351−356.

(22) Liao, C. J.; Lin, F. H.; Chen, K. S.; Sun, J. S. Thermal Decomposition and Reconstitution of Hydroxyapatite in Air Atmosphere. *Biomaterials* **1999**, *20*, 1807−1813.

(23) Liang, S. C.; Chang, Z. C.; Tsai, D. C.; Lin, Y. C.; Sung, H. S.; Deng, M. J.; Shieu, F. S. Effects of Substrate Temperature on the Structure and Mechanical Properties of (TiVCrZrHf)N Coatings. *Appl. Surf. Sci.* **2011**, *257*, 7709−7713.

(24) Subramanian, B.; Ananthakumar, R.; Vidhya, V. S.; Jayachandran, M. Influence of Substrate Temperature on the Materials Properties of Reactive DC Magnetron Sputtered Ti/TiN Multilayered Thin Films. *Mater. Sci. Eng. B* **2011**, *176*, 1−7.

(25) Cheng, H.; Wu, A.; Xiao, J.; Shi, N.; Wen, L. Effects of Substrate Temperature on the Growth of Polycrystalline, Si Films Deposited with SiH_4^+Ar. *J. Mater. Sci. Technol.* **2009**, *25*, 489−491.

(26) Hong, S. I.; Seo, Y. S. Effect of Microstructure on Wear Behavior of Al−Mg−Si Alloy Matrix−10 vol.% Al_2O_3 Composite. *Mater. Sci. Eng: A* **1999**, *265*, 29−41.

(27) Hoppe, A.; Will, J.; Detsch, R.; Boccaccini, A. R.; Greil, P. J. Formation and *in Vitro* Biocompatibility of Biomimetic Hydroxyapatite Coatings on Chemically Treated Carbon Substrates. *J. Biomed. Mater. Res. A* **2014**, *102*, 193−203.

(28) Hong, S. I.; Lee, K. H.; Outslay, M. E.; Kohn, D. H. Ultrastructural Analyses of Nanoscale Apatite Biomimetically Grown on Organic Template. *J. Mater. Res.* **2008**, *23*, 478−485.